Science Advances
AAAS

Supplementary Materials for

Predicting optimal mixotrophic metabolic strategies in the global ocean

Holly V. Moeller *et al.*

Corresponding author: Holly V. Moeller, hvmoeller@ucsb.edu

Sci. Adv. **10**, eadr0664 (2024)
DOI: 10.1126/sciadv.adr0664

This PDF file includes:

Supplementary Methods

Optimal allocation

We first consider the two "edge" cases: (1) strict phagotrophy, and (2) strict phototrophy. First, we identify the growth-maximizing strategies under the assumptions of strict investment. Second, we identify cases under which these strategies are universally growth-maximizing.

Case 1: Strict phagotrophy: If an organism abandons photosynthesis (i.e., sets $\alpha_P = 0$), the associated yield matrix $\mathbb{Y}_{phago}$ becomes:

$$\mathbb{Y}_{phago} = \begin{pmatrix} u_{CB}B - r & -r \\ u_{NB}B & 0 \\ 0 & y_{GM} \end{pmatrix} \tag{S1}$$

If bacterial stoichiometry (combined with mixotroph assimilation and growth efficiencies) differs substantially from mixotroph stoichiometry, one of the elemental components (carbon or nitrogen) may be excess. Thus, strictly phagotrophic (and strictly phototrophic) strategies are not necessarily zero-waste strategies (though they will be zero-waste in either C or N). Thus we must consider two equalities:

$$\hat{g}_C = \hat{g}_G \quad \text{or} \quad \hat{g}_N = \hat{g}_G. \tag{S2}$$

From the first equality, we can determine α_{VC}, the investment in vacuoles that results in zero carbon waste:

$$\alpha_{VC} = \frac{q_G y_{GM} + q_C r}{q_C u_{CB} B + q_G y_{GM}}. \tag{S3}$$

From the second equality, we can obtain α_{VN}, the vacuole investment that results in zero nitrogen waste:

$$\alpha_{VN} = \frac{q_G y_{GM}}{q_N u_{NB} B + q_G y_{GM}}. \tag{S4}$$

The maximum of these two α values defines the phagotroph's growth-maximizing investment strategy and identifies the elemental component that limits growth:

$$\tilde{\alpha}_V = \max(\alpha_{VC}, \alpha_{VN}), \tag{S5}$$

$$\tilde{\alpha}_P = 0, \tag{S6}$$

$$\tilde{\alpha}_M = 1 - \tilde{\alpha}_V. \tag{S7}$$

If $\alpha_{VC} > \alpha_{VN}$, growth is carbon limited, and if $\alpha_{VN} > \alpha_{VC}$, growth is nitrogen limited. We define $\tilde{g}_{CV}$ and $\tilde{g}_{NV}$ as the corresponding per-biomass fluxes of carbon and nitrogen in a strict phagotroph:

$$\tilde{g}_{CV} = q_C \left(u_{CB} B \tilde{\alpha}_V - r\right) \tag{S8}$$

$$\tilde{g}_{NV} = q_N u_{NB} B \tilde{\alpha}_V. \tag{S9}$$

The overall per-biomass growth rate $\tilde{g}$ will be:

$$\tilde{g} = q_G y_{GM} \left(1 - \tilde{\alpha}_V\right). \tag{S10}$$

Case 2: Strict phototrophy: Alternatively, if the organism is strictly phototrophic, it will have a yield matrix:

$$\mathbb{Y}_{photo} = \begin{pmatrix} u_{CL} L - r & -r \\ u_{NI} I & 0 \\ 0 & y_{GM} \end{pmatrix}, \tag{S11}$$

an associated investment strategy:

$$\bar{\alpha}_V = 0, \tag{S12}$$

$$\bar{\alpha}_P = \max\left(\frac{q_G y_{GM} + q_C r}{q_C u_{CL} L + q_G y_{GM}}, \frac{q_G y_{GM}}{q_N u_{NI} I + q_G y_{GM}}\right), \tag{S13}$$

$$\bar{\alpha}_M = 1 - \bar{\alpha}_P, \tag{S14}$$

per-biomass C and N fluxes:

$$\bar{g}_{CP} = q_C \left(u_{CL} L \bar{\alpha}_P - r \right) \tag{S15}$$

$$\bar{g}_{NP} = q_N u_{NI} I \bar{\alpha}_P, \tag{S16}$$

and growth rate:

$$\bar{g} = q_G y_{GM} \left(1 - \tilde{\alpha}_P \right). \tag{S17}$$

Rules for selecting special cases: There are three scenarios in which strict phagotrophy is optimal:

- Phagotrophy has higher carbon and nitrogen yields. That is, $u_{CB} B > u_{CL} L$ and $u_{NB} B > u_{NI} I$.
- The growth rate with the phagotrophic strategy is higher than the growth rate with the phototrophic strategy ($\tilde{g} > \bar{g}$) and
  - either the phagotrophic strategy is carbon limited and phagotropy has higher carbon yield than phototrophy ($u_{CB} B > u_{CL} L$),
  - or the phagotrophic strategy is nitrogen limited and phagotropy has higher nitrogen yield than phototrophy ($u_{NB} B > u_{NI} I$).

In such cases, the optimal investment strategy $\vec{\alpha}^* = (\tilde{\alpha}_V, 0, 1 - \tilde{\alpha}_V)$, and the per-biomass growth rate is $g^* = \tilde{g} = q_G y_{GM} \left(1 - \tilde{\alpha}_V \right)$.

Similarly, there are three scenarios in which strict phototrophy is optimal:

- Phototrophy has higher carbon and nitrogen yields. That is, $u_{CL} L > u_{CB} B$ and $u_{NI} I > u_{NB} B$.

- The growth rate with the phototrophic strategy is higher than the growth rate with the phagotrophic strategy ($\bar{g} > \tilde{g}$) and
  - either the phototrophic strategy is carbon limited and phototrophy has higher carbon yield than phagotrophy ($u_{CL}L > u_{CB}B$),
  - or the phototrophic strategy is nitrogen limited and phototrophy has higher nitrogen yield than phagotrophy ($u_{NI}I > u_{NB}B$).

In such cases, the optimal investment strategy $\vec{\alpha}^* = (0, \bar{\alpha}_P, 1 - \bar{\alpha}_P)$, and the per-biomass growth rate is $g^* = \bar{g} = q_G y_{GM} (1 - \bar{\alpha}_P)$.

In all other cases, mixotrophy is optimal.

Case 3: Mixotrophy. We determine a mixotroph's growth-maximizing investment strategy $\vec{\alpha}^*$ based on two assertions: (1) that, when $\vec{\alpha}$ is fixed, the proportions of the three structures V, P, and M converge on α_V, α_P, and α_M, respectively, over time, and (2) that a growth-maximizing mixotrophic investment strategy is also a zero-waste strategy.

Assertion 1: Structure relative abundances converge on investment strategies. The dynamics of the three mixotroph structures are given by:

$$\frac{dV}{dt} = \alpha_V g \tag{S18}$$

$$\frac{dP}{dt} = \alpha_P g \tag{S19}$$

$$\frac{dM}{dt} = \alpha_M g \tag{S20}$$

where the growth rate g is determined by C, N, and G fluxes from each structure type:

$$\begin{aligned} g_C &= q_C(u_{CB}BV + u_{CL}LP - r(V+P+M)) \\ g_N &= q_N(u_{NB}BV + u_{NI}IP) \\ g_G &= q_G y_{GM} M \\ g &= \min(g_C, g_N, g_G)\,. \end{aligned} \tag{S21}$$

Let us assume that the proportion of digestive vacuoles in an organism is given by ρ_V, such that:

$$\rho_V = \frac{V}{V+P+M}. \tag{S22}$$

Then,

$$V = \rho_V\,(V+P+M)\,. \tag{S23}$$

Differentiating by time, we obtain:

$$\frac{dV}{dt} = \rho_V \left(\frac{dV}{dt} + \frac{dP}{dt} + \frac{dM}{dt}\right) \tag{S24}$$

$$\frac{dV}{dt} = \rho_V\,(\alpha_V g + \alpha_P g + \alpha_M g) \tag{S25}$$

$$\frac{dV}{dt} = \rho_V g\,(\alpha_V + \alpha_P + \alpha_M)\,. \tag{S26}$$

Recalling that $\alpha_V + \alpha_P + \alpha_M = 1$, it is clear that the proportion ρ_V must equal α_V to satisfy the equality. We confirmed this assertion numerically (Figure S1).

Once the cell structures have converged on their relative proportions, the fluxes of each component into the cell *per unit organismal biomass* are given by:

$$\hat{g}_C = q_C(u_{CB}B\alpha_V + u_{CL}L\alpha_P - r) \tag{S27}$$

$$\hat{g}_N = q_N(u_{NB}B\alpha_V + u_{NI}I\alpha_P) \tag{S28}$$

$$\hat{g}_G = q_G y_{GM}\alpha_M, \tag{S29}$$

and the per-biomass growth rate $\hat{g}$ is the minimum of these.

Assertion 2: The growth-maximizing solution is the zero-waste solution. For an optimally growing mixotroph, maximum growth rates should occur when $\hat{g}_C = \hat{g}_N = \hat{g}_G$. With an investment strategy that satisfies this equality, the mixotroph is balancing investments in C acquisition, N acquisition, and growth factor production such that all three components are equally available to support growth. This is a no-waste solution: there is no surplus of any component, and thus growth rate is maximized. We confirmed this assertion numerically (Figure S2).

Equating the per-biomass growth fluxes of all three components gives us a system of three equations with two unknowns (α_V and α_P, since $\alpha_M = 1-\alpha_V-\alpha_P$). We can solve algebraically to find the growth-maximizing strategy $\vec{\alpha}^*$:

$$\alpha_V^* = \frac{q_C(q_G y_{GM}(r - u_{CL}L) + r u_{NI} q_N I) + q_G y_{GM} u_{NI} q_N I}{q_C(q_G y_{GM}(u_{CB}B - u_{CL}L) + q_N B(u_{CB}u_{NI}I - u_{CL}u_{NB}L)) + q_G y_{GM} q_N (u_{NI}I - u_{NB}B)}, \tag{S30}$$

$$\alpha_P^* = \frac{q_C(q_G y_{GM}(r - u_{CB}B) + r u_{NB} q_N B) + q_G y_{GM} u_{NB} q_N B}{q_C(q_G y_{GM}(u_{CL}L - u_{CB}B) + q_N B(u_{CL}u_{NB}L - u_{CB}u_{NI}I)) + q_G y_{GM} q_N (u_{NB}B - u_{NI}I)} \tag{S31}$$

$$\alpha_M^* = 1 - \alpha_V^* - \alpha_P^*. \tag{S32}$$

This growth-maximizing strategy holds when $\alpha_V, \alpha_P > 0$.

MOCHA in a chemostat

To assess how mixotroph strategies change in response to dynamic feedbacks on the resource environment, we simulated a mixotroph growing in a chemostat-like environment with a dilution rate D, an ambient light level L, inorganic nutrients I that inflow at a base concentration I_0, and bacterial prey B that inflow at a base concentration B_0. For simplicity, we assumed that bacteria do not grow independently in the chemostat (but note that this assumption does not meaningfully change the conclusions of our analysis).

We assume that mixotrophs impact their resources in the following ways: First, they graze down bacteria with an attack rate a. Thus, the dynamics of the bacteria are given by:

$$\frac{dB}{dt} = D\,(B_0 - B) - aVB, \tag{S33}$$

where V is the amount (in biomass) of mixotroph vacuoles. The carbon and nitrogen acquisition rates from the bacteria arise from the attack rate, with $u_{CB} = af_C$ (where f_C is the amount of assimilated carbon per bacterium) and $u_{NB} = af_N$ (where f_N is the amount of assimilated nitrogen per bacterium).

Second, the mixotrophs draw down inorganic nutrients through a similar dynamic:

$$\frac{dI}{dt} = u_{NI} I P, \tag{S34}$$

where P is the amount (in biomass) of mixotroph plastids.

Third, the mixotrophs (and all other components in the chemostat) reduce the light field from an input light level L_0 following the Beer-Lambert law, with component-specific absorptivities κ_X:

$$L = L_0 \exp\left(-\kappa_0 - \kappa_V V - \kappa_P P - \kappa_M M - \kappa_B B - \kappa_I I\right). \tag{S35}$$

We model the mixotroph's optimal strategy as described by the MOCHA model above, and modify the dynamics of the mixotroph biomass pool to include dilution within the chemostat:

$$\frac{dV}{dt} = \alpha_V g - DV \tag{S36}$$

$$\frac{dP}{dt} = \alpha_P g - DP \tag{S37}$$

$$\frac{dM}{dt} = \alpha_M g - DM. \tag{S38}$$

This formulation allowed us to simulate changes in the mixotroph's strategy as its activity fed back on resource availability. At the start of each numerical simulation, we initialized the mixotroph with $\vec{\alpha^*}$ calculated based on initial resource availability (L_0, I_0, and B_0), and with initial abundances of V, P, and M proportional to the optimal strategy. We then simulated the chemostat model forward in time until the system reached its asymptotic equilibrium. In our numerical simulations (e.g., Figures S3-S4), we observed three scenarios in which the mixotroph's strategy was stable (i.e., no changes in α_V^*, α_P^*, and α_M^* over a window of time). Each of these stable periods is separated by a region of dynamic change in strategies and resource availability.

1. Initial phase of exponential growth (quasi-equilibrium). For a window of time during initial resource drawdown, the mixotroph population grows exponentially. The optimal strategy is identical to the initial strategy, as the mixotroph draws down resources proportionally to its balanced C and N acquisition. V, P, and M grow at the same rate (the mixotroph's maximum growth rate) and remain proportional to the optimal investment strategy.

2. Secondary phase of exponential growth (second quasi-equilibrium; not present in all simulations, but see Figure S4). In some cases, the mixotroph eventually alters the resource landscape sufficiently that two strategies (typically one mixotrophic, and one strictly phagotrophic or strictly phototrophic) become near-identical (i.e., the growth rates for each strategy are growth-maximizing and typically within 10^{-4} of one another). In these regions of resource space, the mixotroph has essentially found a discontinuity in strategy space, and exhibits "bang-bang" dynamics as it oscillates between the two strategies (*49*). The effect of this bang-bang control is that one of the mixotroph's structures remains constant over time, as resources continue to be drawn down. The system eventually enters a period of transition before ultimately reaching steady-state dynamics.

3. Equilibrium (steady state). After sufficient time, the mixotroph reaches equilibrium, and there is no longer any change in biomass or resource availability. At this point, the mixotroph's growth-maximizing investment strategy is also stable, although we note that at this point the mixotroph's growth rate is also by definition equal to the dilution rate of the chemostat. As described by Klausmeier et al. (*24, 25*), under these circumstances, the MOCHA algorithm of maximizing biomass is unlikely to be biologically realistic, because a hypothetical population would, under these circumstances, be under selection to maximize competitive ability by drawing down resources to their minimal level. Thus, we do not consider this equilibrium outcome further.

Experimental data generation

We used data previously collected in our laboratory using eight isolates (a.k.a. "strains") of *Ochromonas* (*27*). A full description of experimental methods is given in (*27*). Briefly, eight *Ochromonas* strains originally isolated from the Western North Atlantic (Strains 1392 and 1393), the North Atlantic oligotrophic gyre (Strains 584, 590, 1148, 1150, and 1391), and the Western North Pacific (Strain 2951) were ordered from the National Center for Marine Microalgae and Microbiota (Bigelow Labs, USA). A culture of each strain was acclimated to one of seven light levels ranging from 0 to 150 μmol quanta m^{-2} s^{-1}. After at least two weeks of acclimation time, growth, photosynthetic capacity, and grazing were assayed. All experiments were conducted in triplicate. Growth rates were estimated as the slope of a linear model relating the natural log of population sizes (enumerated daily) over time. Photosynthetic capacity was assessed through chlorophyll extraction (quantifying chlorophyll per cell, a proxy for photosynthetic investment) and fluorescence methods (estimating electron transport through photosystem II, a proxy for photosynthetic carbon fixation rate). We used fluorescently labeled bacteria, offered to *Ochromonas* cultures at a range of different initial concentrations, to determine the Holling Functional Response (*50*), from which we estimated attack rates (a proxy for phagotrophic investment) and grazing rates at bacterial abundance in each culture (a proxy for the rate of phagotrophy). To link our resource acquisition rate measurements to *Ochromonas* growth, we used carbon and nitrogen cellular content estimates for bacterial (*29*) and *Ochromonas* (*27*) cultures grown in our lab. (Because our *Ochromonas* cultures are xenic, we corrected for bacterial contributions to carbon and nitrogen using data on mean bacterial cellular carbon and nitrogen content and bacterial abundance.)

While Barbaglia et al. (*27*) include two bacterial abundance treatments in their study, here we used only the data from the low (ambient) bacterial treatment, and excluded the high bacterial treatment data. We made this choice for several reasons. First, the high bacterial treatment was created through the addition of a grain of sterile rice to each culture flask. (This is a fairly standard method for increasing organic carbon in the media, thus stimulating bacterial growth and increasing the food supply for bacterivorous protists like *Ochromonas*.) We wished to avoid confounding factors like undescribed changes to the relative composition of the bacterial community that would be created by this supplementation. Second, the low bacterial treatment is

more representative of bacterial concentrations in the ocean. Third, estimates of resource acquisition rates via phagotrophy in the high bacterial regime suggested that *Ochromonas* in these environments would need to rely very little on photosynthesis. Thus, in these experiments, the presence of photosystems may have been more representative of a constraint on phenotypic plasticity (e.g., the inability to fully eliminate photosystems) as opposed to evidence of a balanced nutritional strategy. Because our focus was on the optimality of mixotrophy, we therefore focused on the low-bacterial experiments.

Model fitting

To fit the model to the experimental data, we set up relations between the model quantities and the experimentally observed quantities in Table S1.

Hereby we used that the allocation vector equals the steady state of relative organelle proportions (as described before). The parameters w_V, w_P and w_{PI} are quantities that describe the relation between model quantities and observed quantities. We fit those parameters together with the other model parameters in the likelihood function.

Before fitting the model, we fixed some of the parameters for which we had direct estimates in order to reduce the number of free parameters. The fixed parameters and the (known) environmental factors are shown in Table S2.

The parameters that need to be fit are shown in Table S3.

Likelihood function We estimate the parameter values by maximizing a likelihood function. The approach is described in detail in Jager & Ashauer (*45*). We fit a separate set of parameters for each strain of *Ochromonas*. Additionally, we fit a set of parameters for all data combined, irrespective of the strain (to get a rough estimate of an "average" *Ochromonas* strain).

We use the following four measured quantities: $\Omega = \{$attack rate, grazing rate, chlorophyll, photosynthesis rate, growth rate$)\}$. For each measurement, we additionally know the corresponding light level.

For each type of data $\omega \in \Omega$, we calculate the sum of squared differences between data and model:

$$s_\omega = \sum_{i=1}^{\lambda_\omega} \left(x_{\omega,i} - \hat{x}_{\omega,i}\right)^2 \tag{S39}$$

where λ_ω is the number of data points for this quantity, $x_{\omega,i}$ is the i'th data point and $\hat{x}_{\omega,i}$ is the corresponding model prediction, assuming that the allocation into the different structures is optimal (given the light level at that data point).

The contribution of each type of data to the log-likelihood function is

$$\ell_\omega = const_\omega - \frac{\lambda_i}{2} \log(s_i) \tag{S40}$$

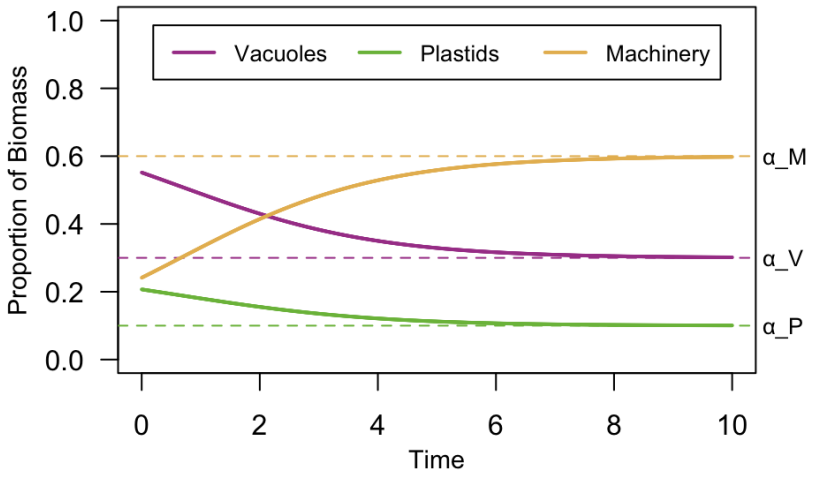

Figure S1: **Convergence of structure proportions on α values**. Solid lines represent simulated trajectories of the relative abundances of vacuoles (magenta), plastids (green), and growth machinery (yellow) over time. (Relative abundance of, e.g., vacuoles is given by $V/(V+P+M)$.) Over time, the proportions of all three structures converge on their respective α values (marked with dashed horizontal lines in corresponding colors).

where $const_\omega$ is a constant that does not depend on the parameters and can be ignored for optimization. The final log-likelihood function is

$$\ell_{total} = \sum_{\omega \in \Omega} \ell_\omega \tag{S41}$$

We maximize this likelihood function to find estimates for the parameter values. The values for u_{CB}, u_{CL}, u_{NB}, and y_{GM} are shown in Figure 3. The values for the other parameters are saved in a spreadsheet online and can be found at https://zenodo.org/doi/10.5281/zenodo.13826163. This spreadsheet also lists the bacteria densities B used in the experiments and the fitting for each strain.

To confine the parameter space, we added the following constraints: $1 \leq y_{GM} \leq 2$, $5 \times 10^{-8} \leq u_{CB} \leq 2 \times 10^{-7}$, $7.5 \times 10^{-8} \leq u_{NB} \leq 3 \times 10^{-7}$, $0.01 \leq u_{CL} \leq 0.04$, $0.01 \leq w_{PL} \leq 0.04$, $3.6 \times 10^{-6} \leq w_V \leq 1.4 \times 10^{-5}$, $20 \leq w_P \leq 80$.

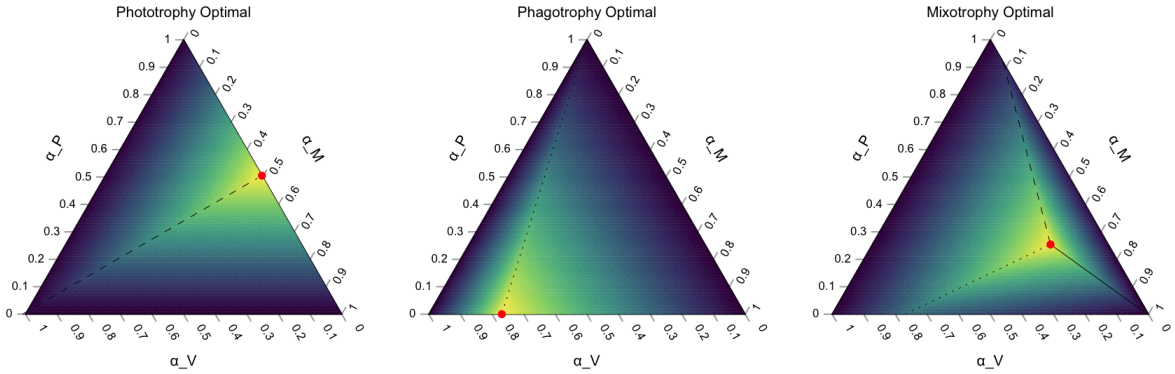

Figure S2: **Determining optimal investment strategies.** Ternary plots show heatmaps of growth rate as a function of the three-structure investment strategy (dark blue = slow or negative growth; yellow = fast growth). Lines indicate strategies that produce equivalence of growth components: Solid lines represent $\hat{g}_C = \hat{g}_N$, dashed lines represent $\hat{g}_C = \hat{g}_G$, and dotted lines represent $\hat{g}_N = \hat{g}_G$. Note that when strict phagotrophy or strict phototrophy are optimal, only one of these equalities is true. The growth-maximizing strategy is at the convergence point of the lines (or, in the cases of strict phagotrophy or phototrophy, where the non-optimal metabolic investment is set to zero).

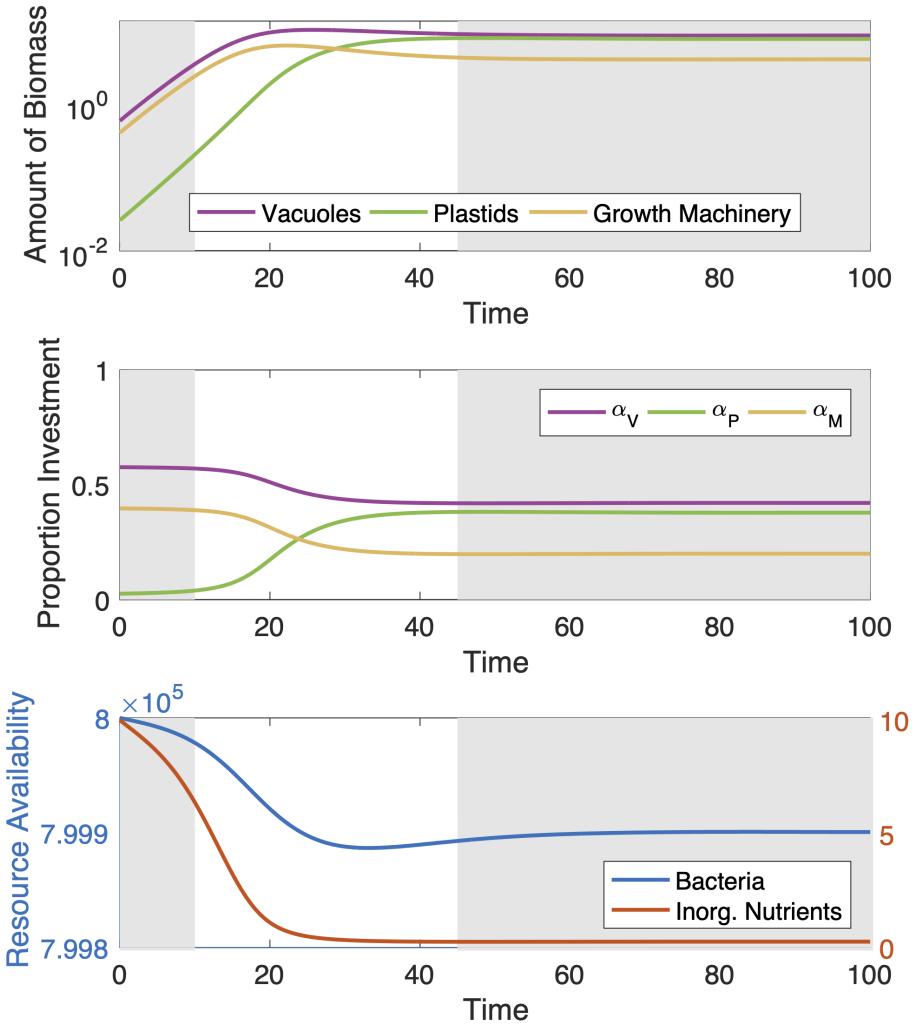

Figure S3: **Mixotroph optimal strategies in a chemostat.** We initialized our chemostat model with strategies and structural biomass assigned by MOCHA optimization based on initial resource values. Over an initial, exponential growth window (leftmost gray background, until $t = 10$), the mixotroph followed this strategy until resources were sufficiently depleted. This triggered a transition period (white background), before the mixotroph reached equilibrium (a.k.a. steady-state) dynamics (rightmost gray background, beginning at $t = 45$). Parameter values were $L_0 = 50$, $I_0 = 10$, $B_0 = 0.8x10^6$, $r = 1$, $y_{GM} = 1$, $u_{CL} = 0.01$, $u_{NI} = 1$, $a = 0.000003$, $f_C = 1$,$f_N = 0.1$,$q_C = q_N = q_G = 1$, $D = 0.2$, $\kappa_X = 0$.

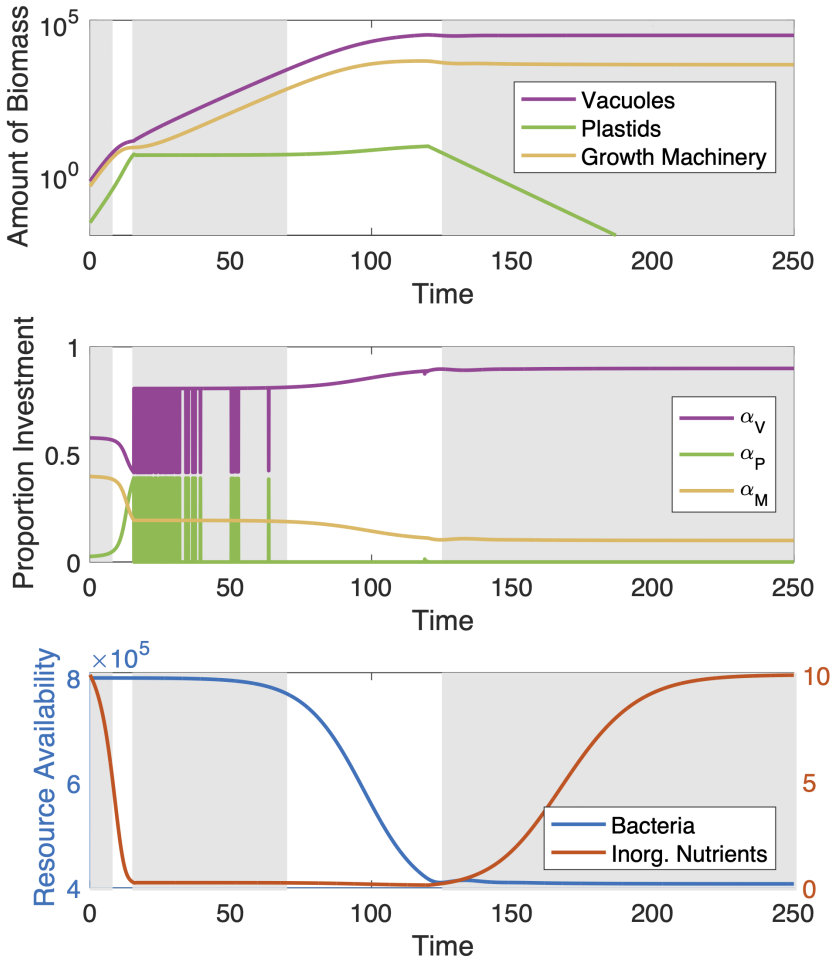

Figure S4: **Mixotroph optimal strategies in a chemostat with transition to strict phagotrophy.** By decreasing the dilution rate of the chemostat ($D = 0.1$; all other parameters the same as Figure S3), we obtained a mixotroph that went through five distinct phases of growth in the chemostat. First (leftmost gray background), the mixotroph followed the initial strategy, until reaching a transition point during which nutrients were depleted (first white background). In the second quasi-equilibrium (middle gray background), the mixotroph exhibited a "bang-bang" control, in which it alternated between mixotrophic and strictly phagotrophic investments, resulting in the maintenance of a near-constant amount of plastids in the chemostat. Over time, bacteria were sufficiently depleted until the mixotroph entered the second transitionary phase (white background) when substantial depletion of the bacteria necessitated investment in a strictly phagotrophic strategy. This strict phagotrophy persisted as the mixotroph achieved steady-state (rightmost gray background), even as nutrients were replenished to input concentrations.

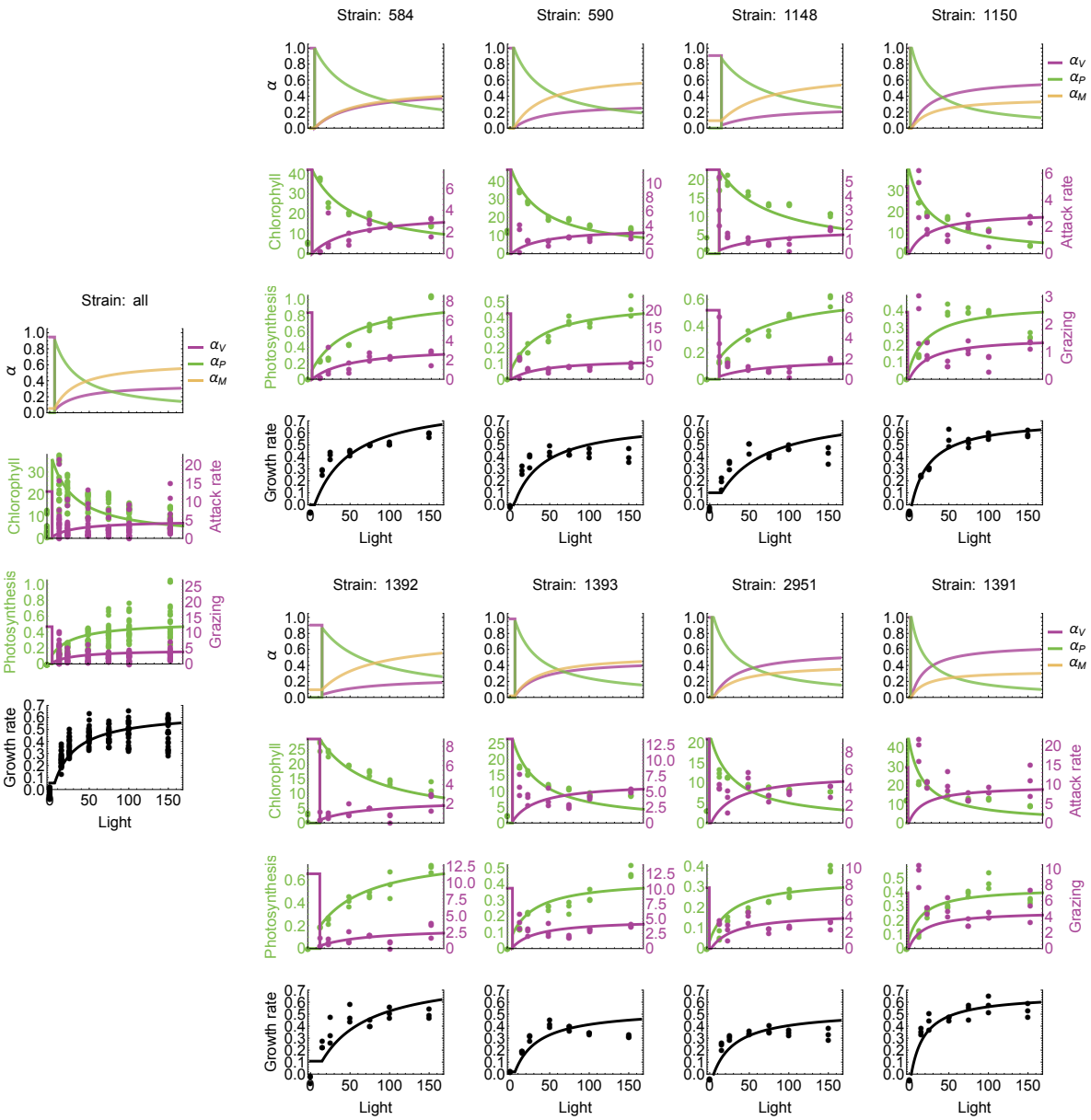

Figure S5: **Model fits for all strains.** For each strain, we show how the model predictions (lines) change with the light level (μmol quanta m^{-2} s^{-1}). Each strain panel shows the follwing. Top plot: optimal investments. Second row: chlorophyll per *Ochromonas* biomass (mgChl gC^{-1}) and attack rate, a.k.a. "clearance rates," in units of mL per *Ochromonas* biomass per day (mL gC^{-1} day^{-1}). Third row: photosynthesis rate as carbon fixated per *Ochromonas* biomass per day (gC gC^{-1} day^{-1}) and the grazing rate, a.k.a. "ingestion rates," in units of bacteria per *Ochromonas* per day (CFU μgC^{-1} day^{-1}). Final row: growth rate per day (day^{-1}). The dots show the experimental data points to which we fit the model.

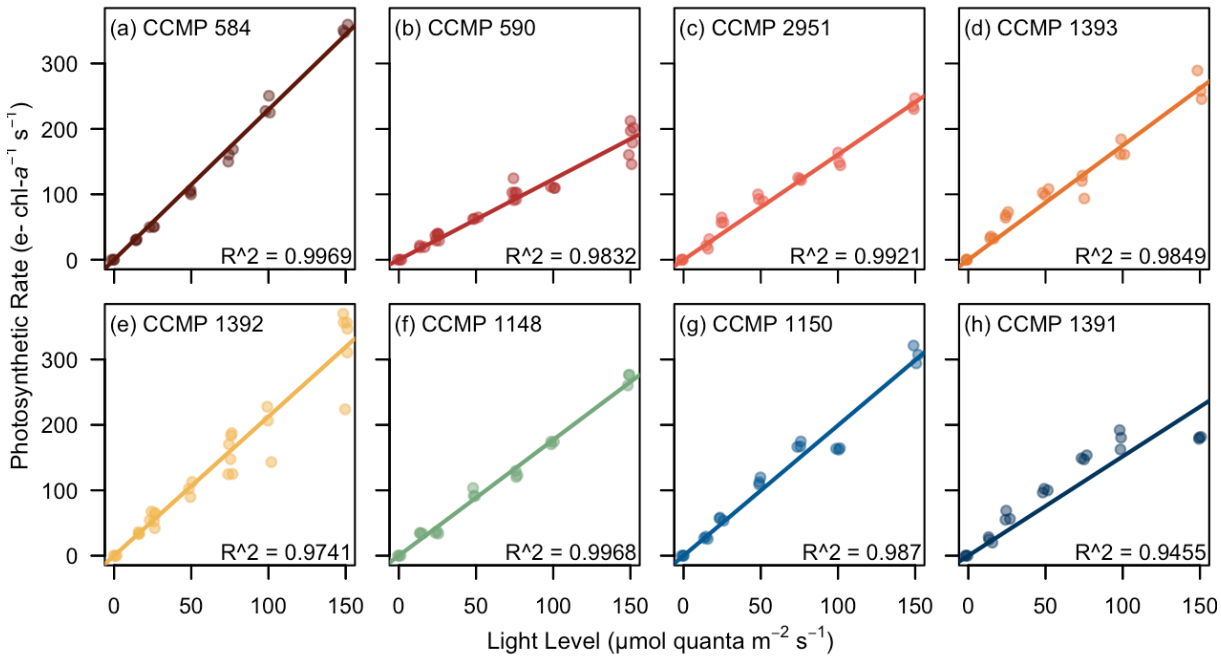

Figure S6: **Increases in per-chlorophyll photosynthetic rates with light for the eight *Ochromonas* strains used in this study.** Data are from Barbaglia et al. (*27*), but have been replotted here with linear trendlines. Although per-cell photosynthetic rates tend to be a saturating function of light (which was also true in Barbaglia et al. (*27*)), this saturation coincides with reductions in chlorophyll content per cell. Thus, in our data, the amount of light harvested per photosystem remained a linear function of light intensity in almost all cases (but see likely saturation of CCMP 1391; panel h).

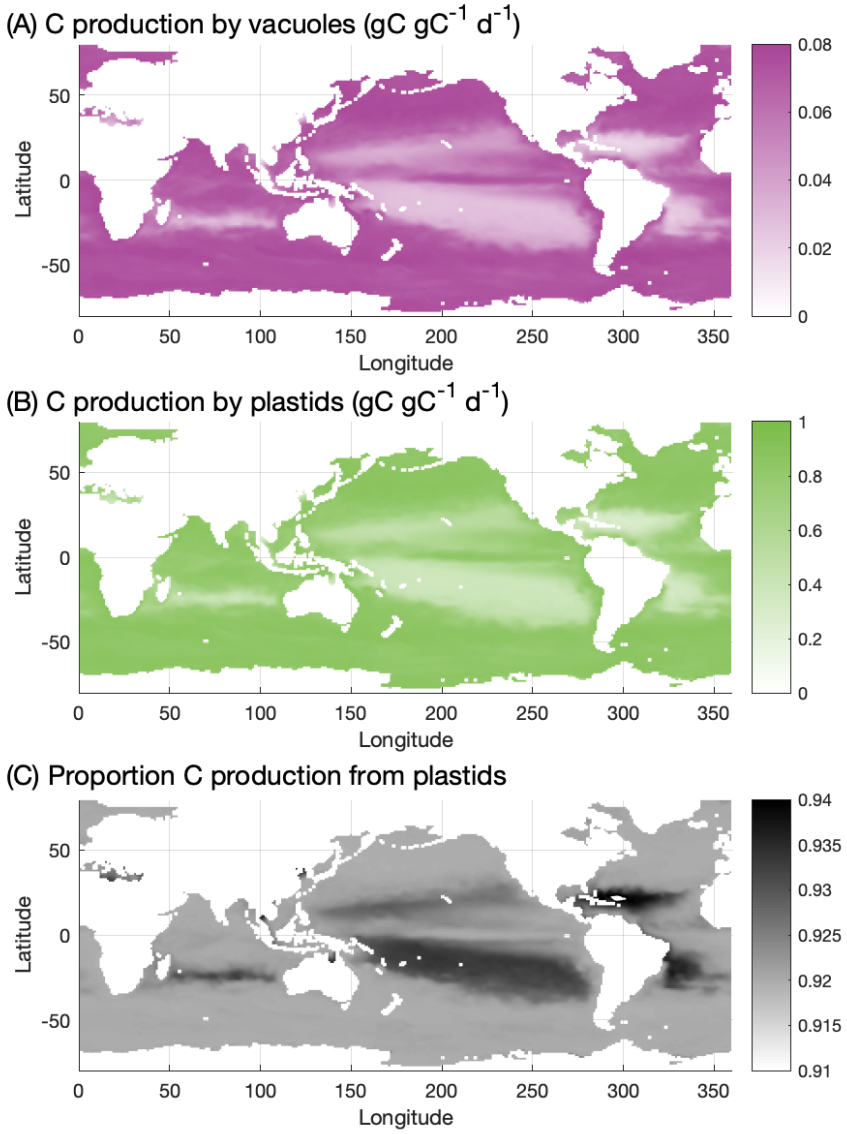

Figure S7: **Carbon production by strategy at the global scale.** Because growth-maximizing strategies are zero-waste strategies, carbon production is proportional to growth (Figure 4F), with the highest production in temperate and polar latitudes and the lowest production in the oligotrophic gyres. Production by plastids via photosynthesis was generally ≈15-fold higher, such that >90% of mixotrophs' C acquisition was via plastids. This percentage was slightly higher in the oligotrophic gyres where low bacterial abundance reduced C and N uptake from bacteria despite high investments in digestive vacuoles. Results are from simulations based on an average *Ochromonas* strain.

Table S1: **Relations between the model quantities and the experimentally observed quantities.**

Quantity	Equation	Units
Attack rate per biomass C	$w_V \alpha_V$	mL^{-1} gC^{-1} day^{-1}
Grazing rate per biomass C	$w_V \alpha_V B$	CFU μgC^{-1} day^{-1}
Chlorophyll per biomass C	$w_P \alpha_P$	mgChl gC^{-1}
Photosynthesis per biomass C	$w_{PI} \alpha_P$	gC gC^{-1} day^{-1}
Growth rate	$g = y_{GM} \alpha_M$ [1]	day^{-1}

[1] This holds with optimal allocation.

Table S2: **Fixed parameters used in model simulations.**

Symbol	Value	Description	Units	Source
q_N	10	C-N ratio of *Ochromonas*	gC gN^{-1}	(*29*)
q_C	1	C-C ratio of *Ochromonas*	gC gC^{-1}	This holds trivially
q_G	1	Quota for growth factor of *Ochromonas*	gC day^{-1}	This quota can be chosen arbitrarily (it scales the fit parameter y_{GM})
r	0.1	Basal respiration per C biomass	gC gC^{-1} day^{-1}	Within the range reported in (*51*)
u_{NI}	0	Nitrogen uptake parameter for plastids per C plastid structure	L day^{-1} gC^{-1}	Assumed to be negligible
I	0	Inorganic nitrogen	gN L^{-1}	Irrelevant because inorganic nitrogen cannot be taken up ($u_{NI} = 0$)
B	approx. 10^6	Bacterial density	CFU mL^{-1}	Has been counted for each strain (same for all light levels)
L	0-150	Light intensity	μmol quanta m^{-2} s^{-1}	Fixed in experimental design

Table S3: **Parameters that are fit to experimental data.**

Symbol	Description	Units
w_V	Maximal attack rate per C	mL gC^{-1} day^{-1}
w_P	Maximal chlorophyll per C	mgChl gC^{-1}
w_{PI}	Maximal per light photosynthesis for relating to photosynthesis data C per C plastid structure per light	gC gC^{-1} day^{-1} (μmol quanta m^{-2} s^{-1})$^{-1}$
y_{GM}	Maximal growth rate in C per C growth structure	gC gC^{-1} day^{-1}
u_{CL}	Maximal per light photosynthesis for model fluxes in C per C per light	gC gC^{-1} day^{-1} (μmol quanta m^{-2} s^{-1})$^{-1}$
u_{CB}	Bacteria to carbon uptake parameter in C per C vacuole structure per time and bacteria density	gC gC^{-1} day^{-1} (CFU mL^{-1})$^{-1}$
u_{NB}	Bacteria to nitrogen uptake parameter in C per C vacuole structure per time and bacteria density	gN gC^{-1} day^{-1} (CFU mL^{-1})$^{-1}$

REFERENCES AND NOTES

1. A. Z. Worden, M. J. Follows, S. J. Giovannoni, S. Wilken, A. E. Zimmerman, P. J. Keeling, Rethinking the marine carbon cycle: Factoring in the multifarious lifestyles of microbes. *Science* **347**, 1257594 (2015).

2. M.-A. Selosse, M. Charpin, F. Not, Mixotrophy everywhere on land and in water: The grand écart hypothesis. *Ecol. Lett.* **20**, 246–263 (2017).

3. J. Tittel, V. Bissinger, B. Zippel, U. Gaedke, E. Bell, A. Lorke, N. Kamjunke , Mixotrophs combine resource use to outcompete specialists: Implications for aquatic food webs. *Proc. Natl. Acad. Sci. U.S.A.* **100**, 12776–12781 (2003).

4. K. W. Crane, J. P. Grover, Coexistence of mixotrophs, autotrophs, and heterotrophs in planktonic microbial communities. *J. Theor. Biol.* **262**, 517–527 (2010).

5. A. Mitra, K. J. Flynn, J. M. Burkholder, T. Berge, A. Calbet, J. A. Raven, E. Granéli, P. M. Glibert, P. J. Hansen, D. K. Stoecker, F. Thingstad, U. Tillmann, S. Våge, S. Wilken, M. V. Zubkov, The role of mixotrophic protists in the biological carbon pump. *Biogeosciences* **11**, 995–1005 (2014).

6. M. Hartmann, C. Grob, G. A. Tarran, A. P. Martin, P. H. Burkill, D. J. Scanlan, M. V. Zubkov, Mixotrophic basis of Atlantic oligotrophic ecosystems. *Proc. Natl. Acad. Sci. U.S.A.* **109**, 5756–5760 (2012).

7. B. A. Ward, M. J. Follows, Marine mixotrophy increases trophic transfer efficiency, mean organism size, and vertical carbon flux. *Proc. Natl. Acad. Sci. U.S.A.* **113**, 2958–2963 (2016).

8. D. K. Stoecker, P. J. Hansen, D. A. Caron, A. Mitra, Mixotrophy in the marine plankton. *Ann. Rev. Mar. Sci.* **9**, 311–335 (2017).

9. A. Mitra, K. J. Flynn, U. Tillmann, J. A. Raven, D. Caron, D. K. Stoecker, F. Not, P. J. Hansen, G. Hallegraeff, R. Sanders, S. Wilken, G. M. Manus, M. Johnson, P. Pitta, S. Våge, T. Berge, A. Calbet, F. Thingstad, H. J. Jeong, J. A. Burkholder, P. M. Glibert, E. Granéli, V. Lundgren,

Defining planktonic protist functional groups on mechanisms for energy and nutrient acquisition: Incorporation of diverse mixotrophic strategies. *Protist* **167**, 106–120 (2016).

10. A. A. Lie, Z. Liu, R. Terrado, A. O. Tatters, K. B. Heidelberg, D. A. Caron, A tale of two mixotrophic chrysophytes: Insights into the metabolisms of two *Ochromonas* species (chrysophyceae) through a comparison of gene expression. *PLOS ONE* **13**, e0192439 (2018).

11. M. D. Johnson, Inducible mixotrophy in the dinoflagellate *Prorocentrum minimum*. *J. Eukaryot. Microbiol.* **62**, 431–443 (2015).

12. R. W. Sanders, K. G. Porter, D. A. Caron, Relationship between phototrophy and phagotrophy in the mixotrophic chrysophyte *Poterioochromonas malhamensis*. *Microb. Ecol.* **19**, 97–109 (1990).

13. S. Wilken, C. J. Choi, A. Z. Worden, Contrasting mixotrophic lifestyles reveal different ecological niches in two closely related marine protists. *J. Phycol.* **56**, 52–67 (2020).

14. S. G. Leles, J. Bruggeman, L. Polimene, J. Blackford, K. J. Flynn, A. Mitra, Differences in physiology explain succession of mixoplankton functional types and affect carbon fluxes in temperate seas. *Prog. Oceanogr.* **190**, 102481 (2021).

15. K. H. Andersen, D. L. Aksnes, T. Berge, Ø. Fiksen, A. Visser, Modelling emergent trophic strategies in plankton. *J. Plankton Res.* **37**, 862–868 (2015).

16. T. Berge, S. Chakraborty, P. J. Hansen, K. H. Andersen, Modeling succession of key resource-harvesting traits of mixotrophic plankton. *ISME J.* **11**, 212–223 (2017).

17. S. Chakraborty, L. T. Nielsen, K. H. Andersen, Trophic strategies of unicellular plankton. *Am. Nat.* **189**, E77–E90 (2017).

18. A. Calbet, M. Bertos, C. Fuentes-Grunewald, E. Alacid, R. Figueroa, B. Renom, E. Garcés, Intraspecific variability in *Karlodinium veneficum*: Growth rates, mixotrophy, and lipid composition. *Harmful Algae* **10**, 654–667 (2011).

19. K. F. Edwards, Mixotrophy in nanoflagellates across environmental gradients in the ocean. *Proc. Natl. Acad. Sci. U.S.A.* **116**, 6211–6220 (2019).

20. S. G. Leles, A. Mitra, K. J. Flynn, D. K. Stoecker, P. J. Hansen, A. Calbet, G. B. Mc Manus, R. W. Sanders, D. A. Caron, F. Not, G. M. Hallegraeff, P. Pitta, J. A. Raven, M. D. Johnson, P. M. Glibert, S. Våge, Oceanic protists with different forms of acquired phototrophy display contrasting biogeographies and abundance. *Proc. Biol. Sci.* **284**, 20170664 (2017).

21. E. Faure, F. Not, A.-S. Benoiston, K. Labadie, L. Bittner, S.-D. Ayata, Mixotrophic protists display contrasted biogeographies in the global ocean. *ISME J.* **13**, 1072–1083 (2019).

22. S. Wilken, C. C. M. Yung, M. Hamilton, K. Hoadley, J. Nzongo, C. Eckmann, M. Corrochano-Luque, C. Poirier, A. Z. Worden, The need to account for cell biology in characterizing predatory mixotrophs in aquatic environments. *Philos. Trans. R. Soc. B* **374**, 20190090 (2019).

23. N. C. Millette, R. J. Gast, J. Y. Luo, H. V. Moeller, K. Stamieszkin, K. H. Andersen, E. F. Brownlee, N. R. Cohen, S. Duhamel, S. Dutkiewicz, P. M. Glibert, M. D. Johnson, S. G. Leles, A. E. Maloney, G. B. Mcmanus, N. Poulton, S. D. Princiotta, R. W. Sanders, S. Wilken, Mixoplankton and mixotrophy: Future research priorities. *J. Plankton Res.* **45**, 576–596 (2023).

24. C. A. Klausmeier, E. Litchman, T. Daufresne, S. A. Levin, Optimal nitrogen-to-phosphorus stoichiometry of phytoplankton. *Nature* **429**, 171–174 (2004).

25. C. A. Klausmeier, E. Litchman, S. A. Levin, Phytoplankton growth and stoichiometry under multiple nutrient limitation. *Limnol. Oceanogr.* **49**, 1463–1470 (2004).

26. D. Tilman, *Resource Competition and Community Structure* (Princeton Univ. Press, 1982), vol. **296**.

27. G. S. Barbaglia, C. Paight, M. Honig, M. D. Johnson, R. Marczak, M. Lepori-Bui, H. V. Moeller, Environment-dependent metabolic investments in the mixotrophic chrysophyte *Ochromonas*. *J. Phycol.* **60**, 170–184 (2024).

28. R. R. Guillard, in *Culture of Marine Invertebrate Animals: Proceedings—1st Conference on Culture of Marine Invertebrate Animals Greenport* (Springer, 1975), pp. 29–60.

29. M. Lepori-Bui, C. Paight, E. Eberhard, C. M. Mertz, H. V. Moeller, Evidence for evolutionary adaptation of mixotrophic nanoflagellates to warmer temperatures. *Glob. Chang. Biol.* **28**, 7094–7107 (2022).

30. NASA Ocean Biology Processing Group, Moderate-resolution imaging spectroradiometer (MODIS) aqua photosynthetically available radiation data; 2022 reprocessing (2022).

31. C. L. Follett, C. L. Follett, S. Dutkiewicz, F. Ribalet, E. Zakem, D. Caron, E. V. Armbrust, M. J. Follows, Trophic interactions with heterotrophic bacteria limit the range of *Prochlorococcus*. *Proc. Natl. Acad. Sci. U.S.A.* **119**, e2110993118 (2022).

32. P. Abrams, The functional responses of adaptive consumers of two resources. *Theor. Popul. Biol.* **32**, 262–288 (1987).

33. K. F. Edwards, Q. Li, K. A. McBeain, C. R. Schvarcz, G. F. Steward, Trophic strategies explain the ocean niches of small eukaryotic phytoplankton. *Proc. R. Soc. B* **290**, 20222021 (2023).

34. S. Våge, M. Castellani, J. Giske, T. F. Thingstad, Successful strategies in size structured mixotrophic food webs. *Aquat. Ecol.* **47**, 329–347 (2013).

35. B. A. Ward, S. Dutkiewicz, A. D. Barton, M. J. Follows, Biophysical aspects of resource acquisition and competition in algal mixotrophs. *Am. Nat.* **178**, 98–112 (2011).

36. C. J. Choi, V. Jimenez, D. M. Needham, C. Poirier, C. Bachy, H. Alexander, S. Wilken, F. P. Chavez, S. Sudek, S. J. Giovannoni, A. Z. Worden, Seasonal and geographical transitions in eukaryotic phytoplankton community structure in the Atlantic and Pacific oceans. *Front. Microbiol.* **11**, 542372 (2020).

37. J. Frias-Lopez, A. Thompson, J. Waldbauer, S. W. Chisholm, Use of stable isotope-labelled cells to identify active grazers of picocyanobacteria in ocean surface waters. *Environ. Microbiol.* **11**, 512–525 (2009).

38. Q. Li, K. F. Edwards, C. R. Schvarcz, K. E. Selph, G. F. Steward, Plasticity in the grazing ecophysiology of *Florenciella* (Dichtyochophyceae), a mixotrophic nanoflagellate that consumes *Prochlorococcus* and other bacteria. *Limnol. Oceanogr.* **66**, 47–60 (2021).

39. S. Wilken, J. Huisman, S. Naus-Wiezer, E. Van Donk, Mixotrophic organisms become more heterotrophic with rising temperature. *Ecol. Lett.* **16**, 225–233 (2013).

40. L. M. Gonzalez, S. R. Proulx, H. V. Moeller, Modeling the metabolic evolution of mixotrophic phytoplankton in response to rising ocean surface temperatures. *BMC Ecol. Evol.* **22**, 136 (2022).

41. H. H. Kim, C. Laufkötter, T. Lovato, S. C. Doney, H. W. Ducklow, Projected 21st-century changes in marine heterotrophic bacteria under climate change. *Front. Microbiol.* **14**, 1049579 (2023).

42. D. L. Kirchman, X. A. G. Morán, H. Ducklow, Microbial growth in the polar oceans—Role of temperature and potential impact of climate change. *Nat. Rev. Microbiol.* **7**, 451–459 (2009).

43. D. Straile, Gross growth efficiencies of protozoan and metazoan zooplankton and their dependence on food concentration, predator-prey weight ratio, and taxonomic group. *Limnol. Oceanogr.* **42**, 1375–1385 (1997).

44. P. G. Falkowski, J. A. Raven, *Aquatic Photosynthesis* (Princeton Univ. Press, 2013).

45. T. Jager, R. Ashauer, *Modelling survival under chemical stress: A comprehensive guide to the GUTS framework* (Toxicodynamics Ltd., 2018).

46. K. M. Archibald, S. Dutkiewicz, C. Laufkötter, H. V. Moeller, Thermal responses in global marine planktonic food webs are mediated by temperature effects on metabolism. *J. Geophys. Res. Oceans* **127**, e2022JC018932 (2022).

47. N. Cermak, J. W. Becker, S. M. Knudsen, S. W. Chisholm, S. R. Manalis, M. F. Polz, Direct single-cell biomass estimates for marine bacteria via Archimedes' principle. *ISME J.* **11**, 825–828 (2017).

48. A. E. White, S. J. Giovannoni, Y. Zhao, K. Vergin, C. A. Carlson, Elemental content and stoichiometry of sar11 chemoheterotrophic marine bacteria. *Limnol. Oceanogr. Lett.* **4**, 44–51 (2019).

49. L. M. Sonneborn, F. S. Van Vleck, The bang-bang principle for linear control systems. *J. Soc. Ind. Appl. Math. Ser. A Control* **2**, 151–159 (1964).

50. C. S. Holling, Some characteristics of simple types of predation and parasitism. *Can. Entomol.* **91**, 385–398 (1959).

51. M. T. Auer, B. Forrer, Development and parameterization of a kinetic framework for modeling light-and phosphorus-limited phytoplankton growth in cannonsville reservoir. *Lake Reserv. Manag.* **14**, 290–300 (1998).